

PAPER

Application of helium line intensity ratio spectroscopy to xenon plasma in $E \times B$ Penning discharge

To cite this article: Hokuto Sekine *et al* 2024 *Plasma Sources Sci. Technol.* **33** 045004

View the [article online](#) for updates and enhancements.

You may also like

- [Helium Ionization in the Diffuse Ionized Gas Surrounding UCH II Regions](#)
D. Anish Roshi, E. Churchwell and L. D. Anderson
- [More Evidence for Variable Helium Absorption from HD 189733b](#)
Michael Zhang, P. Wilson Cauley, Heather A. Knutson *et al.*
- [ON EXTREME-ULTRAVIOLET HELIUM LINE INTENSITY ENHANCEMENT FACTORS ON THE SUN](#)
A. S. Giunta, A. Fludra, A. C. Lanzafame *et al.*



Analysis Solutions for your Plasma Research

- Knowledge
- Experience ■ Expertise

[Click to view our product catalogue](#)

Contact Hiden Analytical for further details:
www.HidenAnalytical.com
info@hiden.co.uk



Surface Science

- ▶ Surface Analysis
- ▶ SIMS



Surface Science

- ▶ 3D depth Profiling
- ▶ Nanometre depth resolution



Plasma Diagnostics






- ▶ Plasma characterisation
- ▶ Customised systems to suit plasma Configuration



Plasma Diagnostics

- ▶ Mass and energy analysis of plasma ions
- ▶ Characterisation of neutrals and radicals

Application of helium line intensity ratio spectroscopy to xenon plasma in $E \times B$ Penning discharge

Hokuto Sekine^{1,*} , Ahmed Diallo³ , Shota Abe³ , Yevgeny Raitses³ 
and Hiroyuki Koizumi^{1,2} 

¹ Department of Aeronautics and Astronautics, The University of Tokyo, Tokyo, Japan

² Department of Advanced Energy, The University of Tokyo, Chiba, Japan

³ Princeton Plasma Physics Laboratory, Princeton, NJ 08543, United States of America

E-mail: h.sekine@al.t.u-tokyo.ac.jp

Received 7 September 2023, revised 16 February 2024

Accepted for publication 27 March 2024

Published 5 April 2024



Abstract

We propose the application of helium line intensity ratio spectroscopy in a low-pressure (0.3 mTorr) xenon $E \times B$ discharge with an electron temperature of ~ 2 eV and a density of $10^{10} - 10^{11} \text{ cm}^{-3}$. We successfully identified the helium atom line emissions at 388.9, 447.1, 501.6, 504.8, and 706.5 nm with helium pressures of up to ~ 20 mTorr. The measured electron temperature, density, and $I-V$ characteristics of the discharge remained almost constant in all helium pressures in the present experiment, indicating the suitability of the helium gas as a diagnostic gas. The results of helium line intensity ratio spectroscopy using the line emissions at 388.9, 447.1, and 504.8 nm showed fair agreement with the Langmuir probe measurement. Considering the trade-off relationship between the disturbance introduced by the helium gas and the signal-to-noise ratio, we conclude that a helium pressure of approximately 4 mTorr (approximately 13 times the partial pressure of xenon) represents the optimal pressure range for the application of the helium line emission intensity ratio method to this xenon plasma. It is found that the use of the line emissions at 501.6 and 706.5 nm result in a significant disturbance in the helium line intensity ratio method due to the radiation trapping effect.

Keywords: low temperature plasmas, plasma spectroscopy, $E \times B$ discharge, Hall thrusters, helium line intensity ratio spectroscopy

1. Introduction

Helium line emission intensity ratio (LIR) spectroscopy has been applied to determine electron temperatures and densities in fusion and linear devices with background helium plasmas [1–9]. The intensity ratio of emission lines emitted by helium atoms in the plasma is a function of both electron temperature and electron density. Therefore, these parameters can be determined by comparing the measured intensity ratio with a value calculated on the basis of a specific population model of excited levels. The selection of an appropriate model depends

on the dominant energy-transfer process. Corona model has been used for measurement in low-density ($< 5 \times 10^{10} \text{ cm}^{-3}$) plasmas [2, 10, 11], where radiative energy transfer is dominant. In contrast, local thermodynamic equilibrium, where collisional energy transfer is dominant, is often assumed in high-density plasmas ($> 10^{13} \text{ cm}^{-3}$) [12]. Collisional radiative (CR) models, which calculate population distributions by solving rate equations that account for collisional and radiative transitions, have often been used for plasmas of moderate density ($10^{10} - 10^{12} \text{ cm}^{-3}$).

Partially magnetized plasmas in cross-field discharge devices are used for a variety of applications, including electric propulsion and plasma processing [13, 14]. There are unresolved mechanisms that cause a variety of turbulent

* Author to whom any correspondence should be addressed.

fluctuations and structures [15, 16], and they are still being investigated because they critically affect the performance of those devices [17, 18]. Measurements of plasma parameters are vital for comprehending them and assessing device performance, and spectroscopic methods stand as a promising approach for evaluating these parameters in a non-invasive manner [19]. Among the various spectroscopy methods, such as laser-induced fluorescence [20–22], laser absorption spectroscopy [23], Thomson scattering [24–27], and so on, optical emission spectroscopy is one of the simplest methods.

Xenon is an often used working gas for these devices due to its large ionization cross sections and the resultant high efficiency [28–30]. In recent years, CR models for xenon [31–36] have been developed, but it remains a challenging issue to construct accurate xenon CR model codes mainly due to their large number of energy levels. On the other hand, as helium has a limited number of energy levels and those cross sections have been precisely obtained, the accuracy of the CR model generally exceeds that of other atoms or molecules.

In this paper, we propose the utilization of helium LIR spectroscopy via the emission from helium admixed within a xenon plasma as a diagnostic technique for determining the electron temperature and density of xenon plasmas. To the best of our knowledge, this is the first application of helium LIR spectroscopy in a helium-xenon mixed plasma. The applicability of this method is evaluated by comparing the electron temperature and density estimated by the helium LIR method with those measured by a Langmuir probe.

2. Method

2.1. CR model

The population densities of the energy levels of helium atoms can be calculated using a CR model [19]. According to the CR model, the time derivative of the population density of the energy level p in the ionization stage 0 (neutral) is expressed by the rate equation taking into account the collisional transition of electrons, radiative transitions out of/into the level p , collisional ionization to the ionization stage i , and three-body / dielectronic / radiation recombinations. In steady state, given the ground-state densities of atoms $n_0(g)$ and singly-ionized ions $n_i(g)$, the excited-level population $n_0(p)$ can be written as

$$n_0(p) = C_0(p, T_e, n_e) n_0(g) + C_i(p, T_e, n_e) n_i(g), \quad (1)$$

where T_e and n_e are the electron temperature and electron density, and C_0 and C_i represent the effective upward contribution of the ground state (denoted by the subscript ‘0’) and downward contribution of the ion (denoted by the subscript ‘i’), respectively. Since the first term is dominant in ionizing plasmas [19], the photon emission coefficients ϵ are derived as

$$\epsilon(p \rightarrow q) = h\nu_{pq} A(p \rightarrow q) n_0(p) \quad (2)$$

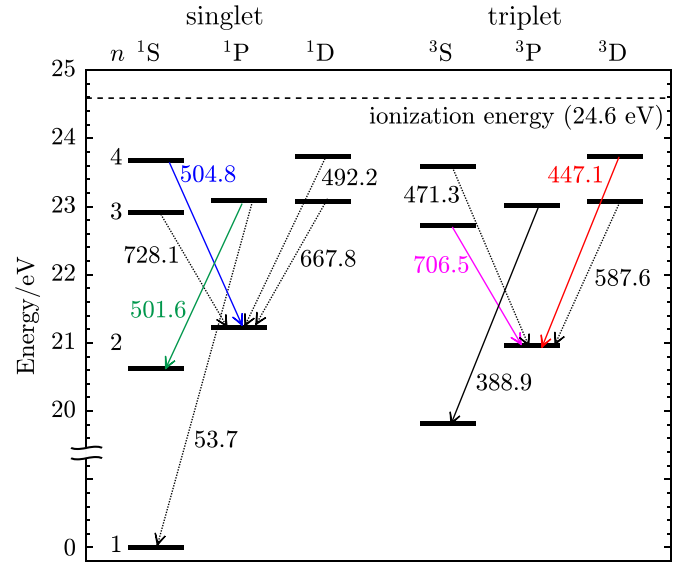


Figure 1. Grotrian diagram of a helium atom for the relevant energy levels. The number next to the arrow indicates the wavelength of the transition in nanometers, and n is the principal quantum number. The five emission lines used in this study (388.9, 447.1, 501.6, 504.8, and 706.5 nm) are highlighted by the colors.

$$= h\nu_{pq} A(p \rightarrow q) C_0(p, T_e, n_e) n_0(g), \quad (3)$$

where h , ν_{pq} , and $A(p \rightarrow q)$ are the Planck constant, the frequency of a radiative transition from level p to level q , and the spontaneous transition probability from p to q , respectively. By taking the ratio of $\epsilon(p \rightarrow q)$ to another photon emission coefficient for a different transition, $\epsilon(p' \rightarrow q')$, one can obtain the line intensity ratio as a function of T_e and n_e , $f(T_e, n_e)$, as

$$\frac{\epsilon(p \rightarrow q)}{\epsilon(p' \rightarrow q')} = \frac{h\nu_{pq} A(p \rightarrow q) C_0(p, T_e, n_e) n_0(g)}{h\nu_{p'q'} A(p' \rightarrow q') C_0(p', T_e, n_e) n_0(g)} \quad (4)$$

$$\equiv f(T_e, n_e). \quad (5)$$

By choosing another intensity ratio, another function of T_e and n_e can be calculated. Once the two intensity ratios are obtained from the measurements, T_e and n_e can be determined as solutions to the simultaneous equations. In this study, we used the CR model available in ADAS [37], where the corresponding data set was pec96#he_pju#he0.dat, as done in [38, 39]. Helium LIR spectroscopy utilizes the difference in the sensitivity of the two functions in T_e and n_e . In other words, the pair of line intensity ratio should be carefully selected, as it is directly related to the measurement uncertainty of T_e and n_e in this method. Since the CR model mentioned above assumes an ionizing plasma, this method is applicable to plasmas with $T_e > 1$ eV and $n_e < 10^{14}$ cm $^{-3}$; beyond this range, the effects of recombination become non-negligible [40].

Previous studies indicated that the kinetic processes of the metastable state atoms may have a significant influence on the CR model under certain plasma conditions [41–43]. This impact should be discussed, where the ADAS CR model does not take these processes into account (equation (1)). Figure 1

illustrates the Grotrian diagram detailing the relevant transitions for helium in this study, where 2^1S and 2^3S are the metastable states. Since the extinction time by electron impact excitation/deexcitation increases significantly with decreasing T_e , metastable state atoms have a relatively long extinction time in low-temperature plasmas [41]. A previous study indicated that the extinction time of metastable state atoms becomes non-negligible compared to the transport timescale of neutrals in the recombining regime, where T_e is much lower than 1 eV [42]. Consequently, metastable state atoms traverse long distances, modifying spatial density profiles. However, since the plasma we study in this paper is typically in the ionizing regime, considering the measured T_e and n_e as will be shown, the transport effect of metastable state atoms can be considered negligible, as demonstrated in [3, 44].

Ionization by collisions with metastable atoms in mixed gases, known as Penning ionization, may also be important as a kinetic effect of metastable atoms [41]. Given that the excitation energy of helium atoms (>21 eV) exceeds the ionization energy of xenon atoms (~ 12.1 eV), collisions with metastable helium can result in the ionization of xenon atoms. We may note that Penning ionization reduces the lifetime of metastable state helium atoms [45], which serves to mitigate the above-mentioned modification of spatial plasma profiles by their transport. The impact of this effect will be experimentally evaluated in section 2.3. Heavy particle collisions, including Penning ionization, can affect the excited populations. This is true for atmospheric low-temperature plasmas but not for mTorr-discharge plasmas. Santos *et al* included these reactions in their CR model for atmospheric pressure plasma applications [46]. Still, they were negligible for mTorr-discharge plasmas because of less presence of metastable compared to atmospheric pressure plasmas.

2.2. Experimental setup

2.2.1. Penning discharge system.

All experiments were conducted in the $E \times B$ Penning system in the Princeton Plasma Physics Laboratory [47–49]. Figure 2 illustrates the schematic of the experimental setup. The Penning system, approximately 26 cm in diameter and 50 cm in length, incorporates a radial electric field and an axial magnetic field that induce electron $E \times B$ drift. Xenon gas was continuously introduced into a radio frequency cathode, resulting in a chamber pressure of 0.3 mTorr, where P_{cham} was measured using a Granville-Phillips, Series 375 Convectron Vacuum Gauge. A discharge voltage V_d was then applied to the cathode with respect to the ground, producing plasma. During the xenon discharge, helium gas was added to the chamber with a pressure P_{cham} of up to ~ 20 mTorr. Here, we define the helium pressure P_{He} as $P_{\text{He}} = P_{\text{cham}} - P_{\text{Xe}}$, where P_{Xe} was the chamber pressure only with xenon gas, which was assumed to remain at 0.3 mTorr. The discharge current I_d and the discharge voltage V_d were kept constant at 1.2 A and 55 V for all experiments presented in this paper, respectively. An axial magnetic field was formed by two water-cooled solenoids placed outside the

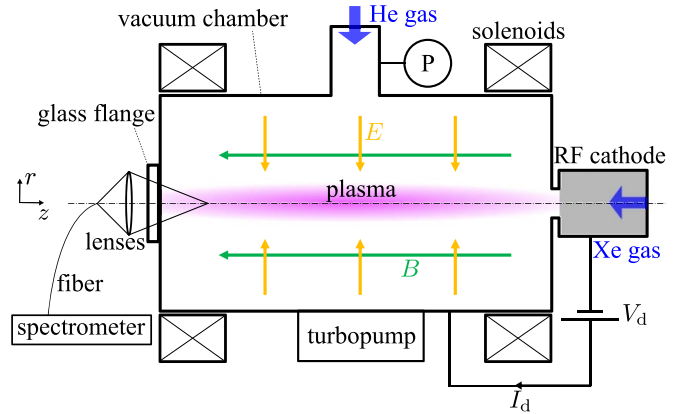


Figure 2. Schematic of the cross-sectional view of the Penning system. It produces the radial electric field E and the axial magnetic field B , inducing particle confinement due to $E \times B$ drift. ‘P’ indicates the vacuum gauge.

chamber, with a strength of ~ 80 G. The typical electron temperature and density are 1–5 eV and $\sim 10^{10} - 10^{11} \text{ cm}^{-3}$ for xenon plasmas in this system [48, 49].

Emission from the plasma on the axis 3 cm away from the glass flange was collected by three 7.5 cm diameter focusing lenses (focal lengths are 2.5, 2.5, and 20 cm, respectively) with an aperture and measured by an Ocean Insight HR2000+ spectrometer, which can obtain spectra in the wavelength range of 380–810 nm at once with 14 bit A/D resolution. Since the magnetic field is almost uniform, we assumed that the plasma is uniform along the axial direction, which is identical to the line-of-sight direction. It should be noted that the axial uniformity of the plasma may be affected by variations in neutral density distribution related to the pump position [50] or non-uniformity induced by the electron beam generated by the biased RF cathode [51]. The photon accumulation time was set to 10 s to obtain sufficient intensities, which means that the present measurements are essentially temporally averaged. The spectrometer was calibrated using conventional calibration lamps both in wavelength and intensity.

2.2.2. Langmuir probe.

To evaluate the applicability of helium LIR spectroscopy in the Penning xenon plasma, we compare the results with those obtained using a Langmuir probe. Measurements of the EEPFs were performed by the VGPS Langmuir probe station described elsewhere [52]. The detection tip of the probe was positioned at the same location as the focal point in the emission spectroscopy measurement, i.e. at a distance of 3 cm from the glass flange. Figure 3(a) shows the measured EEPFs at $P_{\text{He}} = 0.0, 10.0,$ and 20.0 mTorr as representatives. As previously reported [47, 48], the measured EEPFs exhibited bi-Maxwellian-like characteristics, where we can define the temperatures (strictly, mean energies) for the low- and high-energy ranges, $T_{e,\text{low-}E}$ and $T_{e,\text{high-}E}$, respectively.

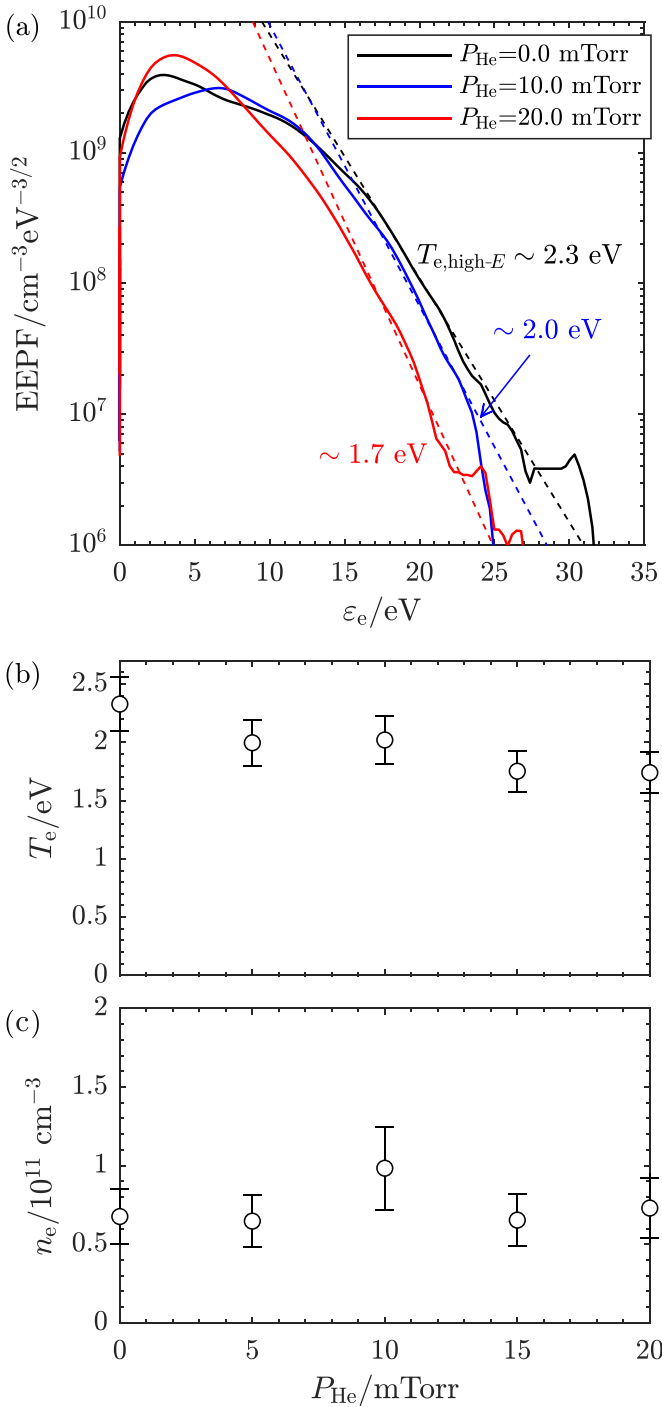


Figure 3. (a) Measured EEPFs at $P_{\text{He}} = 0.0$ (black), 10.0 (blue), and 20.0 (red) mTorr. The electron temperatures of the high-energy range (above ~ 20 eV), $T_{e,\text{high-}E}$, were deduced by linear fits of the EEPFs (dotted lines). Measured (b) electron temperature T_e (strictly, $T_{e,\text{high-}E}$) and (c) density n_e determined by a Langmuir probe as a function of P_{He} .

For comparison with the helium LIR method, the electron temperature in the high-energy range, $T_{e,\text{high-}E}$, is essential. Since the lowest energy that can excite helium atoms is approximately 22 eV, the emission of helium atoms does not include information about $T_{e,\text{low-}E}$, and electrons with kinetic energy below ~ 22 eV only quench via collisions with helium

and xenon atoms. In light of this reason, hereafter, we adopt $T_{e,\text{high-}E}$ as the electron temperature measured by the Langmuir probe T_e . The electron density n_e can be obtained by the integral of an EEPF as

$$n_e = \int_0^{\infty} \varepsilon_e^{1/2} f_p(\varepsilon_e) d\varepsilon_e, \quad (6)$$

where ε_e and f_p are the electron energy and the EEPF, respectively. We take into account the standard deviations as the uncertainties in T_e and n_e .

2.3. Disturbance by the helium gas to the xenon plasma

It is important to clarify the disturbance introduced by the admixed helium gas to the xenon plasma. As mentioned in section 2.2.1, no clear change in the I - V characteristics of the discharge was detected under all experimental conditions. Figures 3(b) and (c) show the dependence of T_e and n_e determined by the Langmuir probe on P_{He} . The measured T_e and n_e were relatively constant with increasing P_{He} , clearly showing the limited disturbance caused by the admixture of helium gas. This is probably due to the high excitation energy of a helium atom, where the bulk electrons collide with the helium atoms elastically, i.e. without losing energy. The unchanged n_e also implies the limited effect of Penning ionization, possibly due to the very small density of the metastable state helium atoms. These characteristics of the helium gas manifest its suitability as a ‘diagnostic gas’ for low-temperature xenon plasmas.

Figure 4 shows the measured spectra at $P_{\text{He}} = 0.0, 5.2$ and 19.7 mTorr. All intensities of the Xe II lines detected in this experiment decreased with P_{He} . This is probably attributed to the depleted energetic tails of the EEPFs shown in figure 3(a). This result also implies the limited impact of Penning ionization. No helium ion emission was detected in the present experiment, indicating that the plasma is primarily a xenon plasma. The representative Xe II emissions as a function of P_{He} is shown in figure 5. Here, $I_{460.30}$, $I_{529.22}$, $I_{533.93}$, $I_{537.24}$, $I_{541.92}$, and $I_{547.26}$ are the measured Xe II line intensities at $\lambda = 460.30, 529.22, 533.93, 537.24, 541.92,$ and 547.26 nm, respectively. Although several emissions (460.30, 537.24, and 547.26 nm) remained almost constant up to $P_{\text{He}} \sim 7$ mTorr, the emission at 529.22 nm was found to be the most sensitive to P_{He} , where the decrease exceeds 10% when $P_{\text{He}} > 4.2$ mTorr.

There exists a trade-off between the disturbance and the signal-to-noise ratio, as a high density of helium atoms will lead to increased helium line intensities and a better signal-to-noise ratio. Therefore, the appropriate helium pressure in this method should be determined not only from the disturbance but also from the signal-to-noise ratio in the helium LIR measurement. Further discussion on the signal-to-noise ratio in the helium LIR measurement will be presented in section 3.

3. Results

As shown in figure 4, the He I line emissions at 388.9 ($2^3\text{S}-3^3\text{P}$), 447.1 ($2^3\text{P}-4^3\text{D}$), 501.6 ($2^1\text{S}-3^1\text{P}$), and 706.5

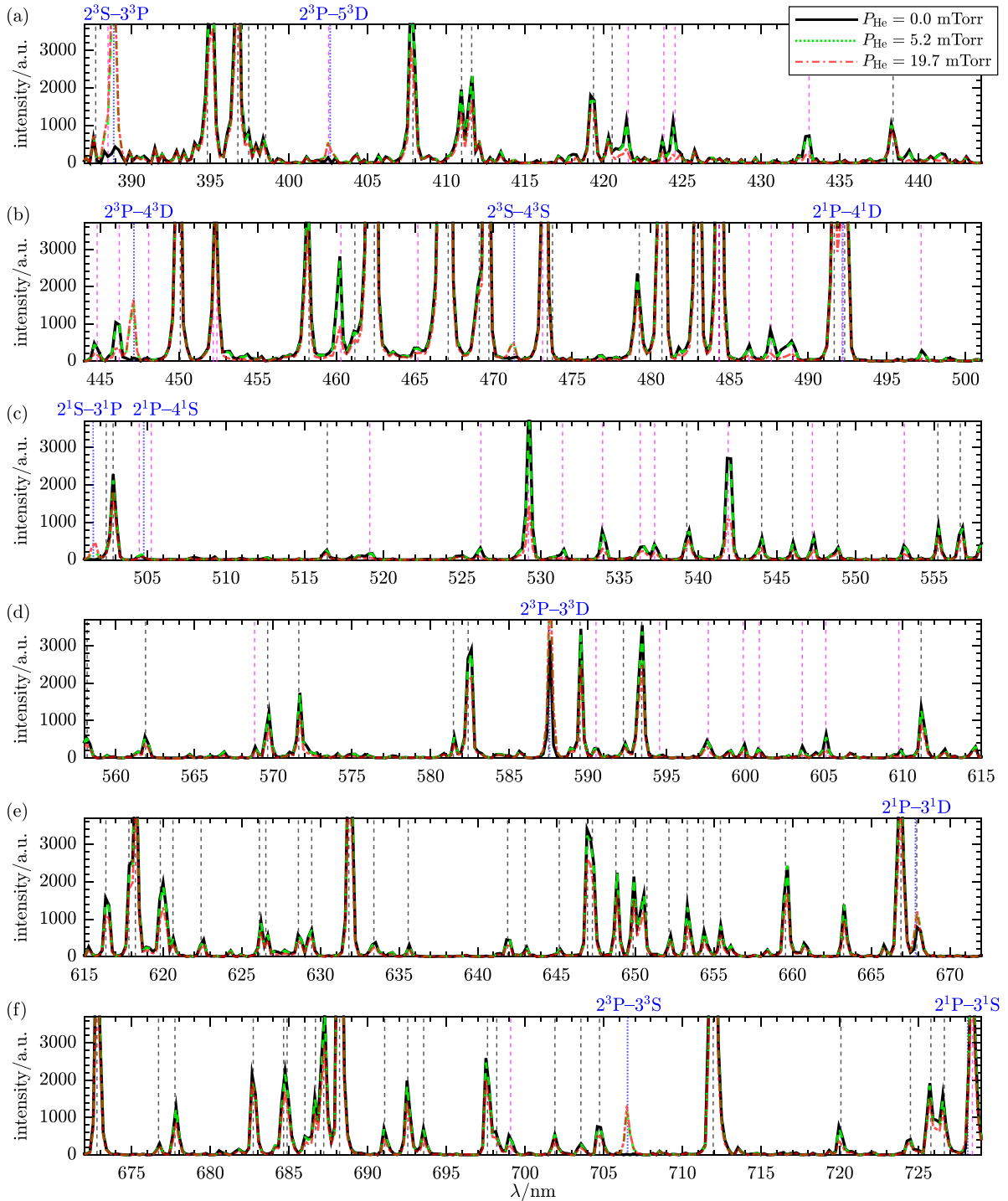


Figure 4. Measured spectra at $P_{\text{He}} = 0.0$ (black solid lines), 5.2 (green dashed lines), and 19.7 mTorr (red dotted lines) in the wavelength range of (a) 387–444, (b) 444–501, (c) 501–558, (d) 558–615, (e) 615–672, and (f) 672–729 nm, respectively. The dashed vertical lines are added at the wavelengths of the Xe I (black), Xe II (magenta), and helium atom lines (blue).

($2^3\text{P}-3^3\text{S}$) nm were clearly identified without significant overlap with the xenon lines. Figure 6 show the fitted spectrum at $P_{\text{He}} = 5.2$ mTorr around 388.9, 447.1, 501.6, 504.8, and 706.5 nm. Careful identification of the He I line at 504.8 nm was necessary by this synthetic analysis due to the partial overlap with a xenon II line at 504.5 nm ($5p^4(^1\text{D}^2)6p-5p^4(^1\text{D}^2)6s$). All fitted Gaussians exhibited an approximate constant value of ~ 0.42 nm full width at half maximum.

Figures 7(a) and (b) show the measured He I intensities and the normalized intensity by the intensity at $P_{\text{He}} = 0.2$ mTorr as a function of P_{He} , respectively. The line intensities at 388.9, 447.1, 504.8, and 706.5 nm peak at $P_{\text{He}} \sim 11$ mTorr. The trend of the line intensity at 501.6 nm is different compared to those lines, where its peak was around $P_{\text{He}} \sim 12$ mTorr. Figure 7(c) shows the variation in intensity ratios as a function of P_{He} . The intensity ratios calculated with the intensities at 388.9, 447.1,

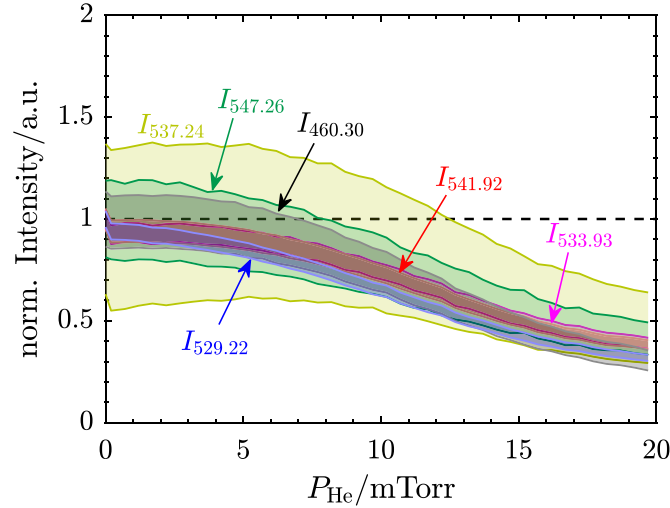


Figure 5. Measured Xe II intensities as a function of P_{He} . They are normalized by the intensities at $P_{\text{He}} = 0.0$ mTorr. The error bars are derived from the 68% confidence intervals of the Gaussian fit to the spectrum and the propagation of uncertainty.

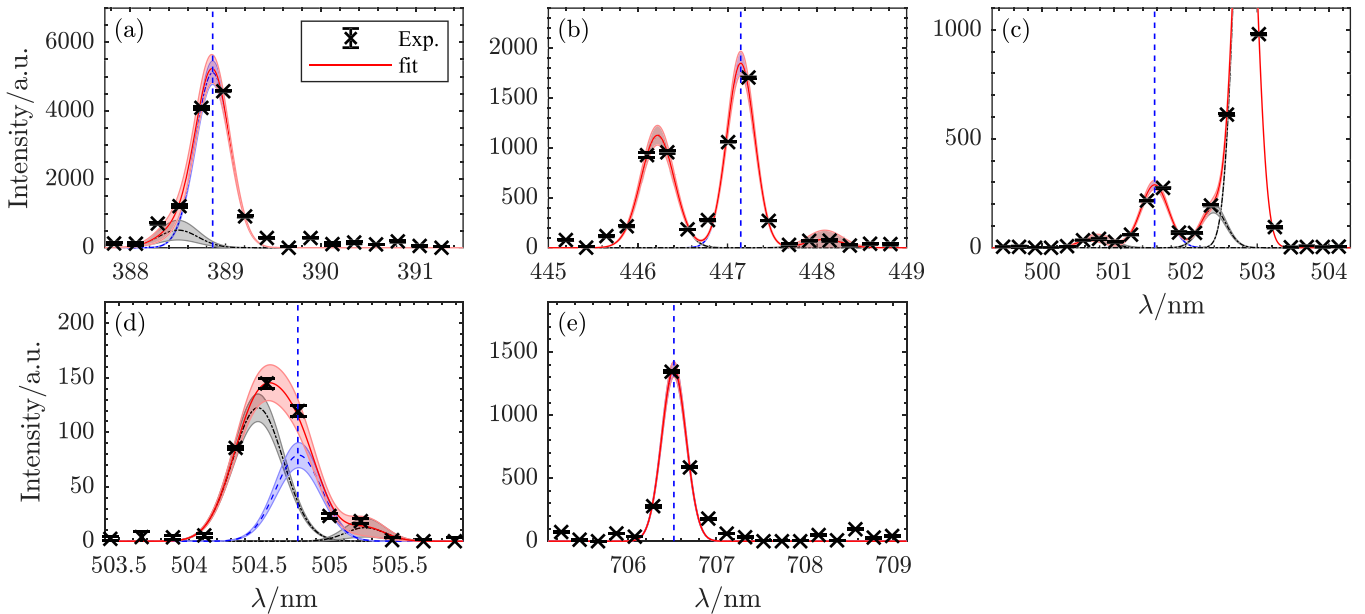


Figure 6. Measured spectra around the (a) 388.9, (b) 447.1, (c) 501.6, (d) 504.8, and (e) 706.5 nm He I lines. The markers show the measured values with the standard errors indicated by the error bars. The blue lines show the fitted Gaussians for the He I lines. The black lines show the fitted Gaussians for the Xe I, Xe II, or Xe III lines. The red line shows the sum of the fitted lines. The shaded regions indicate the 68% confidence intervals.

504.8, and 706.5 nm ($I_{338.9}$, $I_{447.1}$, $I_{504.8}$, $I_{706.5}$) were almost constant within the uncertainty of the measurement. However, the behavior of the intensity ratios was notably dissimilar when using the intensity at 501.6 nm ($I_{501.6}$), which exhibited significant variations in the low-pressure region ($P_{\text{He}} < 5$ mTorr). For subsequent analysis with the CR model, we primarily employed the three line intensity ratios: $I_{338.9}/I_{504.8}$, $I_{447.1}/I_{504.8}$, and $I_{338.9}/I_{447.1}$. The reason for this selection will be discussed in section 4.

Figures 8(a) and (b) depict the measured intensity ratios plotted in the LIR contour maps calculated by the ADAS CR model. In this region such that $T_e < 3$ eV and $n_e < 10^{11}$ cm $^{-3}$,

the calculated intensity ratio $I_{338.9}/I_{447.1}$ was highly sensitive to T_e , while remaining largely unchanged with respect to n_e . As a result, T_e was determined primarily by $I_{338.9}/I_{447.1}$, and n_e was determined by $I_{338.9}/I_{504.8}$ (figure 8(a)) or $I_{447.1}/I_{504.8}$ (figure 8(b)). As can be seen, it was found that even when we use different combinations of LIR (figures 8(a) and (b)), similar values of T_e and n_e were obtained.

Figures 9(a) and (b) show the measured T_e and n_e obtained using the helium LIR method and the Langmuir probe. Again, the results obtained from the different combinations of intensity ratios were found to be in good agreement and consistent with those obtained via the Langmuir probe. The measurement

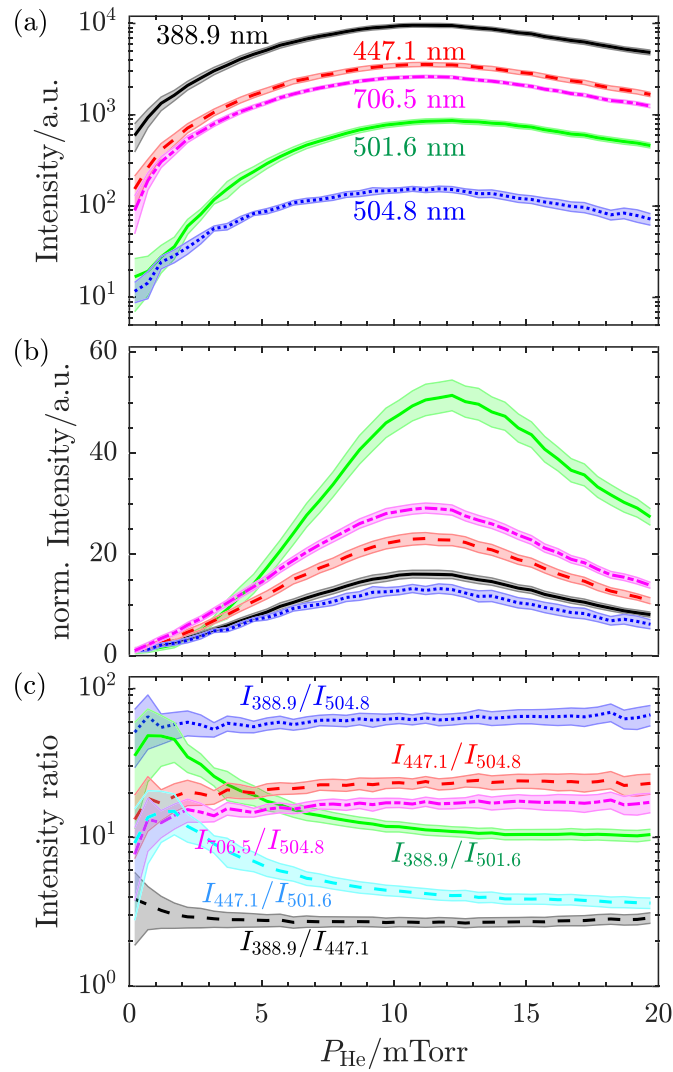


Figure 7. (a) Measured He I intensities as a function of P_{He} on a logarithmic scale. (b) Normalized He I intensities. They are normalized by those at $P_{\text{He}} = 0.2$ mTorr. (c) Intensity ratios as a function of P_{He} . The shaded regions indicate the measurement uncertainties.

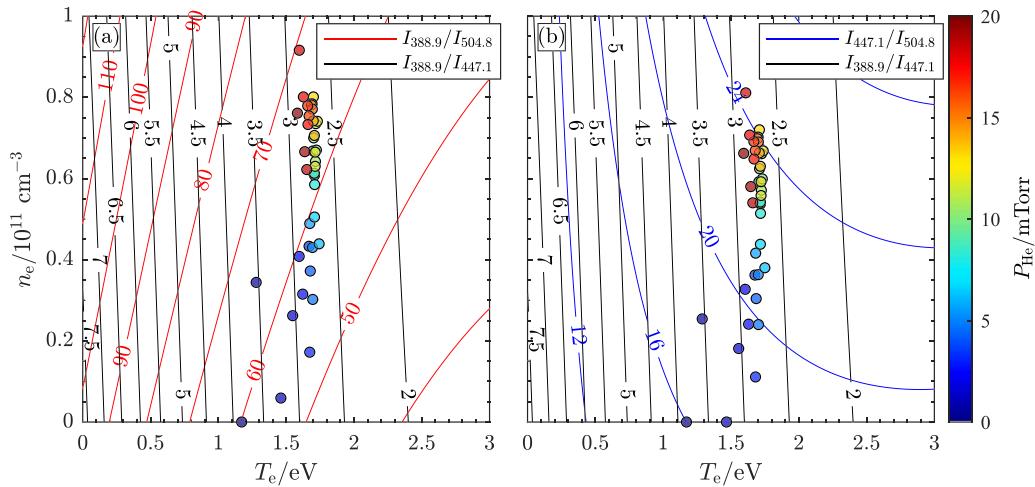


Figure 8. Line intensity ratio contours of (a) $I_{388.9}/I_{504.8}$ and $I_{388.9}/I_{447.1}$ and (b) $I_{447.1}/I_{504.8}$ and $I_{388.9}/I_{447.1}$ calculated by the ADAS CR model. The markers are placed at the intersections of the contour lines whose values correspond to the measured ones, where their colors indicate P_{He} . The error bars are omitted for clarity.

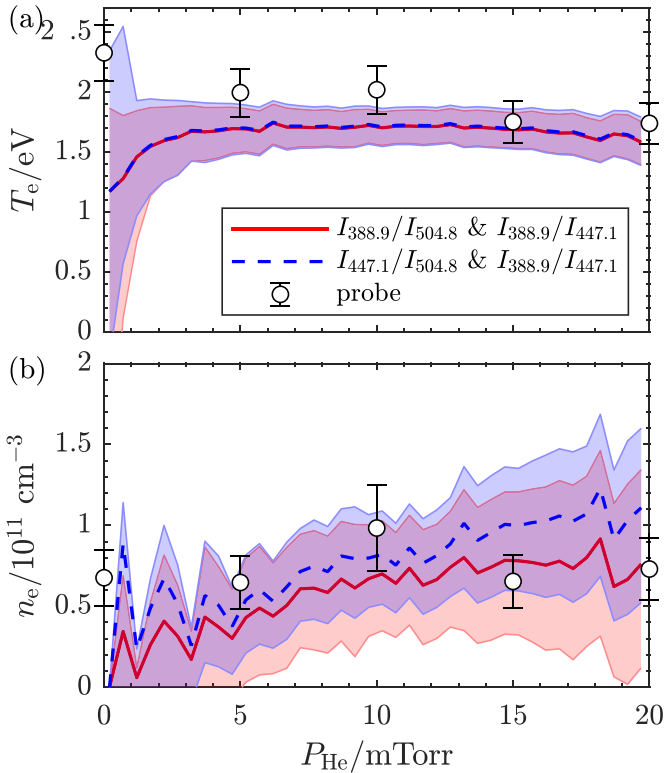


Figure 9. Comparison of the (a) electron temperature T_e and (b) density n_e determined by the helium LIR method and by a Langmuir probe. The shaded regions indicate the measurement uncertainties. The helium LIR method using two LIR combinations (red and blue profiles) showed good agreement with the Langmuir probe measurement results (markers).

uncertainties associated with the helium LIR method for n_e are relatively large ($\pm 55\%$) compared to those for T_e ($\pm 12\%$). This is due to the low sensitivity of the density-determining intensity ratios ($I_{338.9}/I_{504.8}$ and $I_{447.1}/I_{504.8}$) compared to the temperature-determining intensity ratio ($I_{338.9}/I_{447.1}$). The magnitude of the uncertainties also varied with P_{He} . Since the excitation energy of helium significantly exceeds the ionization energy of xenon, the density of the excited helium atom is usually quite low, resulting in poor signal-to-noise ratios for helium emission lines at very low helium pressures. Consequently, the uncertainties in both T_e and n_e are particularly large below ~ 3 mTorr, where they converge to a practical level at $P_{\text{He}} \sim 4$ mTorr or higher. However, as described in section 2.3, the changes in the intensity ratios of the Xe II lines became noticeable with $P_{\text{He}} > 4.2$ mTorr. Hence, we conclude that a helium pressure of ~ 4 mTorr (approximately 13 times the partial pressure of xenon) represents the optimal pressure range for the application of the helium LIR method to ionizing xenon plasmas with $T_e \sim 2$ eV and $n_e \sim 10^{10}$ – 10^{11} cm^{-3} . We may note that the magnitude of these uncertainties is comparable to that of typical Langmuir probe measurements [53].

4. Discussion

In this section, we will discuss the reasons why we could not use the line emissions at 501.6 and 706.5 nm in helium LIR measurements. When we used the visible line emission at 501.6 nm, anomalously high densities were obtained ($> 10^{12}$ cm^{-3}) (not shown). This result suggests that the use of the 501.6 nm line significantly disturbs the measurement of helium LIR under this experimental condition. This is likely due to the phenomenon called radiation trapping, in which background ground-state atoms are photoexcited by reabsorption of the emission from the plasma itself [41]. Since the resonance transitions 1^1S – $n^1\text{P}$, including the 53.7 nm transition (1^1S – 3^1P), are optically connected to the ground level (figure 1), the reabsorption effect on these lines is significant in weakly ionized plasmas [44, 54–56]. As a result of reabsorption on the 53.7 nm transition, the population of the upper level (3^1P) increases, some of which transitions to 2^1P while emitting light at 501.6 nm [44].

The magnitude of radiation trapping is generally represented by the optical depth τ [19]. τ is defined as the spatial integration of the absorption coefficient κ and depends on λ as κ is related to Einstein's B coefficient. In practice, the optical escape factor (OEF) $\Lambda(\tau)$ has been used to take into account the radiation trapping effect in the CR model, by replacing the spontaneous transition probability A with the 'effective' one as ΛA [19]. Note that the OEF does not depend on how we observe the plasma but on the degree of excitation of atoms by the light from the surrounding plasma, and thus, the plasma profile [57–62]. A value of $\Lambda = 1$ indicates that the plasma is completely opaque for the line.

In a cylindrical plasma, the OEF for the line whose lower state is the ground state atom is defined as [41]

$$\Lambda(\tau) \sim \frac{1.92 - 1.3/[1 + \tau^{6/5}]}{(\tau + 0.62)[\pi \ln(1.357 + \tau)]^{1/2}}, \quad (7)$$

where

$$\tau = \kappa R_{\text{OEF}} \quad (8)$$

$$= 1.16546 \times 10^{-8} f(\lambda) \lambda \sqrt{\frac{A_M}{T_p}} n_0 R_{\text{OEF}}. \quad (9)$$

Here, f , A_M , n_0 , and R_{OEF} are the oscillator strength, mass number (4 for helium), density of the ground state atom, and radius of the spatial distribution of the excited atom (so-called the OEF radius), respectively [41]. Figure 10(a) shows the calculated optical depth for the resonance line at 53.7 nm, $\tau_{53.7}$, as a function of P_{He} . As is seen, almost all experiments were performed in an optically thick regime for the 53.7 nm line ($\tau_{53.7} \gg 1$). This violates the assumptions of ordinary CR models, including the ADAS CR model, where $\tau \ll 1$ is assumed for all transitions, i.e. negligible radiation trapping effects. It should be noted that, although the uncertainty of

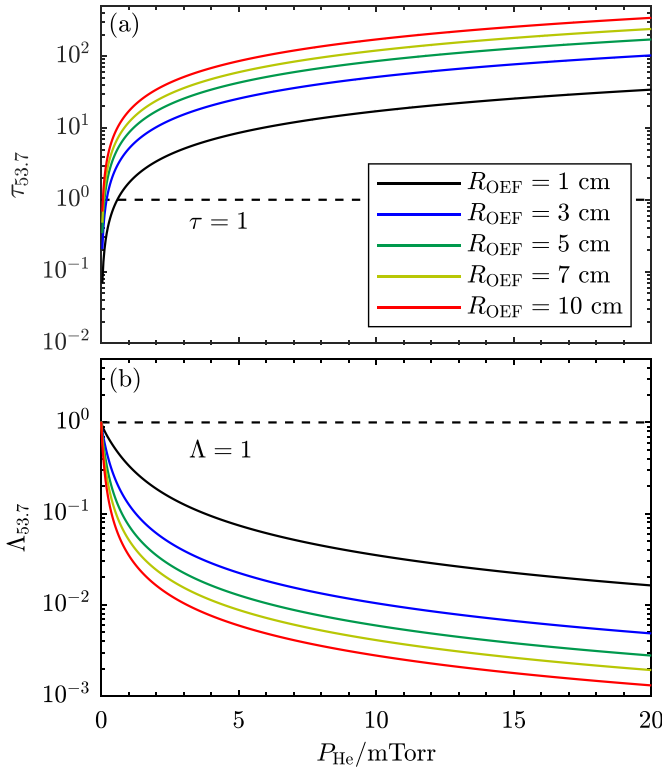


Figure 10. (a) Calculated optical depth of the resonance line at 53.7 nm (3^1P-1^1S) with several OEF radius R_{OEF} as a function of P_{He} . The helium gas temperature was assumed to be 300 K. (b) Calculated OEF for the 53.7 nm line with several R_{OEF} as functions of P_{He} . The dashed line indicates $\Lambda = 1$, which corresponds to the plasma being completely opaque to this line.

τ arises primarily from R_{OEF} , accurate determination of R_{OEF} remains a challenging issue. Therefore, we calculated $\tau_{53.7}$ for several R_{OEF} from 1 cm (smaller than the plasma radius) to 10 cm (approximately the chamber radius) here. Figure 10(b) shows the calculated OEF for the line at 53.7 nm, $\Lambda_{53.7}$. The values of $\Lambda_{53.7}$ show that the effective spontaneous transition probability for this line will be altered up to 10^{-3} times. The distinct behavior of the 501.6 nm line and the anomalous intensity ratios with the 501.6 nm line (figure 7) indicate the significant contribution of the radiation trapping of the 1^1S-3^1P transition. This result is consistent with previous studies that demonstrated that the intensity of the triplet line is less sensitive to radiation trapping than that of the singlet line [55].

The 706.5 nm triplet line was also easily identified (figure 7). This line had high intensity and little overlap with the xenon line, and it is unlikely to be affected much by radiation trapping since it does not share any states with the resonance line optically connected to the ground state. Therefore, this line would seemingly appear suitable for helium LIR spectroscopy in xenon plasmas. However, the line intensity ratios using this line did not give a solution; that is, we were unable to plot the measured line ratios with this line on the calculated intensity ratio contour map (figure 8). A previous study

has reported the anomalous behavior of the 706.5 nm line in a H_2 -He mixed plasma and concluded that using this line perturbs the helium LIR method [43]. Thus, it is possible that the behavior of the 706.5 nm line is not accurately simulated in the ADAS CR model, where the underlying physics that causes those deviations in the CR models remains unresolved at present.

As mentioned above, the line emissions at 501.6 and 706.5 nm were found to disturb the helium LIR measurement employing the ADAS CR model; however, since these emissions are strong and do not overlap with the xenon lines, these features may be useful for real-time (or time-resolved) measurements that do not require any technical fitting analysis. Developing a CR model that incorporates these lines and can be employed for helium-xenon mixed plasmas is a critical future challenge.

5. Conclusion

We proposed the application of helium LIR spectroscopy by mixing helium gas with a xenon $E \times B$ discharge at an electron temperature of ~ 2 eV and an electron density of 10^{10} – 10^{11} cm^{-3} . The measured electron temperature and density were almost constant with the helium pressure, which shows the limited disturbance caused by the introduction of helium gas. This result suggests that the bulk electrons collide elastically with the helium atoms without losing energy, clearly suggesting the suitability of the helium gas as a ‘diagnostic gas’ in low-temperature xenon plasmas.

We successfully identified the helium atom line emissions at 388.9, 447.1, 501.6, 504.8, and 706.5 nm in a wide range of helium pressures. As a result of the analysis of the intensity ratios according to the ADAS CR model, the combinations of 388.9, 447.1, and 504.8 nm lines showed very good agreement with the Langmuir probe, suggesting the applicability of the helium LIR method in a xenon plasma. Since the ADAS CR model we used assumes an ionizing plasma, this method is applicable to plasmas with $T_e > 1$ eV and $n_e < 10^{14}$ cm^{-3} [40]. Considering the trade-off relationship between the disturbance introduced by the helium gas and the signal-to-noise ratio, we conclude that a helium pressure of approximately 4 mTorr (approximately 13 times the partial pressure of xenon) represents the optimal pressure range for the application of the helium LIR method to this xenon plasma.

Regardless of their strong emission without serious overlap with xenon lines, the use of the 501.6 and 706.5 nm lines resulted in a significant disturbance to the helium LIR measurement in the xenon plasma. It is indicated that the radiation trapping effect must be considered to use the 501.6 nm line, as suggested by the previous results [54]. Although the underlying physics is not identified, it was shown that the 706.5 nm line disturbs the helium LIR measurement, as indicated in previous studies. Developing a CR model that incorporates these lines and can be employed for helium-xenon mixed plasmas is a critical future challenge.

Data availability statement

The data that support the findings of this study are available from the corresponding author upon reasonable request.

Acknowledgments

The authors thank Dr Shurik Yatom for fruitful discussions and technical assistance. Hokuto Sekine's work was supported by JSPS KAKENHI Grant Number JP22K18854 and Joint Princeton University—The University of Tokyo program. Ahmed Diallo's, Shota Abe's, and Yevgeny Raitses's works were partially supported by the U.S. Department of Energy through Contract No. DE-AC02-09CH11466.

Author contributions

Hokuto Sekine: Experiment (lead); Formal analysis (lead); Writing—original draft (lead); Writing—review & editing (lead). Ahmed Diallo: Experiment (supporting); Formal analysis (supporting); Writing—review & editing (supporting). Shota Abe: Formal analysis (supporting); Writing—review & editing (supporting). Yevgeny Raitses: Experiment (supporting); Formal analysis (supporting); Writing—review & editing (supporting). Hiroyuki Koizumi: Writing—review & editing (supporting).

Conflict of interest

The authors have no conflicts to disclose.

ORCID iDs

Hokuto Sekine  <https://orcid.org/0000-0002-6140-4450>
 Ahmed Diallo  <https://orcid.org/0000-0002-0706-060X>
 Shota Abe  <https://orcid.org/0000-0002-1477-423X>
 Yevgeny Raitses  <https://orcid.org/0000-0002-9382-9963>
 Hiroyuki Koizumi  <https://orcid.org/0000-0003-0120-1958>

References

- [1] Kubo H, Goto M, Takenaga H, Kumagai A, Sugie T, Sakurai S, Asakura N, Higashijima S and Sakasai A 1999 Study of intensity ratios of He I line (668 nm, 706 nm and 728 nm) for measurement of electron temperature and density in JT-60U divertor plasma *J. Plasma Fusion Res.* **75** 945–66
- [2] Boivin R F, Kline J L and Scime E E 2001 Electron temperature measurement by a helium line intensity ratio method in helicon plasmas *Phys. Plasmas* **8** 5303–14
- [3] Kajita S, Ohno N, Takamura S and Nakano T 2006 Comparison of He I line intensity ratio method and electrostatic probe for electron density and temperature measurements in NAGDIS-II *Phys. Plasmas* **13** 013301
- [4] Schmitz O *et al* (The TEXTOR Team) 2008 Status of electron temperature and density measurement with beam emission spectroscopy on thermal helium at TEXTOR *Plasma Phys. Control. Fusion* **50** 115004
- [5] Ma S, Howard J, Blackwell B D and Thapar N 2012 Measurements of electron density and temperature in the H-1 heliac plasma by helium line intensity ratios *Rev. Sci. Instrum.* **83** 033102
- [6] Lashkul S I, Altukhov A B, D'yachenko V V, Esipov L A, Kantor M Y, Kuprienko D V, Lebedev A D, Nikerman Y A and Popov A Y 2012 Use of additional helium puffing for the diagnostics of plasma parameters at the FT-2 tokamak *Plasma Phys. Rep.* **38** 851–62
- [7] Unterberg E A, Schmitz O, Fehling D H, Stoschus H, Klepper C C, Muñoz-Burgos J M, Van Wassenhove G and Hillis D L 2012 HELIOS: a helium line-ratio spectral-monitoring diagnostic used to generate high resolution profiles near the ion cyclotron resonant heating antenna on TEXTOR *Rev. Sci. Instrum.* **83** 10D722
- [8] Ueda A, Shikama T, Teramoto T, Higashi T, Iida Y and Hasuo M 2018 Helium atom line-intensity ratios as an integrated diagnostic tool for low-pressure and low-density plasmas *Phys. Plasmas* **25** 054508
- [9] Kajita S, Akkermans G, Fujii K, van der Meiden H and van de Sanden M C M 2020 Emission spectroscopy of He lines in high-density plasmas in Magnum-PSI *AIP Adv.* **10** 025225
- [10] Podder N K, Johnson J A, Raynor C T, Loch S D, Ballance C P and Pindzola M S 2004 Helium line intensity ratio in microwave-generated plasmas *Phys. Plasmas* **11** 5436–43
- [11] Lee W, Park K, Kwon D-H and Oh C-H 2016 Optical diagnostics with radiation trapping effect in low density and low temperature helium plasma *Phys. Plasmas* **23** 063516
- [12] Scotti F and Kado S 2009 Comparative study of recombining He plasmas below 0.1 eV using laser Thomson scattering and spectroscopy in the divertor simulator MAP-II *J. Nucl. Mater.* **390–391** 303–6
- [13] Abolmasov S N 2012 Physics and engineering of crossed-field discharge devices *Plasma Sources Sci. Technol.* **21** 035006
- [14] Kaganovich I D *et al* 2020 Physics of $E \times B$ discharges relevant to plasma propulsion and similar technologies *Phys. Plasmas* **27** 120601
- [15] Hara K and Tsikata S 2020 Cross-field electron diffusion due to the coupling of drift-driven microinstabilities *Phys. Rev. E* **102** 023202
- [16] Brown Z A and Jorns B A 2023 Growth and saturation of the electron drift instability in a crossed field plasma *Phys. Rev. Lett.* **130** 115101
- [17] Raitses Y, Kaganovich I D, Khrabrov A, Sydorenko D, Fisch N J and Smolyakov A 2011 Effect of secondary electron emission on electron cross-field current in $E \times B$ discharges *IEEE Trans. Plasma Sci.* **39** 995–1006
- [18] Kim J Y, Choi J, Choi J, Hwang Y S and Chung K-J 2022 Efficiency improvement of an $E \times B$ Penning discharge source by enhanced cross-field transport of electrons *Plasma Sources Sci. Technol.* **31** 05LT02
- [19] Kunze H-J 2009 *Introduction to Plasma Spectroscopy* (Springer)
- [20] Diallo A, Keller S, Shi Y, Raitses Y and Mazouffre S 2015 Time-resolved ion velocity distribution in a cylindrical Hall thruster: heterodyne-based experiment and modeling *Rev. Sci. Instrum.* **86** 033506
- [21] Young C V, Lucca Fabris A, MacDonald-Tenenbaum N A, Hargus W A and Cappelli M A 2018 Time-resolved laser-induced fluorescence diagnostics for electric propulsion and their application to breathing mode dynamics *Plasma Sources Sci. Technol.* **27** 094004
- [22] Doh G, Park J, Lee D, Kim H and Choe W 2021 Determination of the ionization region in Hall thruster plasmas with low perturbation *J. Appl. Phys.* **130** 193301
- [23] Matsui M, Komurasaki K and Arakawa Y 2005 Laser absorption spectroscopy in high enthalpy flows *38th AIAA Thermophysics Conf. (Fluid Dynamics and Co-located*

- Conferences*) (American Institute of Aeronautics and Astronautics)
- [24] Yamamoto N, Tomita K, Sugita K, Kurita T, Nakashima H and Uchino K 2012 Measurement of xenon plasma properties in an ion thruster using laser Thomson scattering technique *Rev. Sci. Instrum.* **83** 073106
- [25] Tsikata S and Minea T 2015 Modulated electron cyclotron drift instability in a high-power pulsed magnetron discharge *Phys. Rev. Lett.* **114** 185001
- [26] Vincent B, Tsikata S, Mazouffre S, Minea T and Fils J 2018 A compact new incoherent Thomson scattering diagnostic for low-temperature plasma studies *Plasma Sources Sci. Technol.* **27** 055002
- [27] Kajita S, Ohshima H, Tanaka H, Seki M, Takano H and Ohno N 2019 Spatial and temporal measurement of recombining detached plasmas by laser Thomson scattering *Plasma Sources Sci. Technol.* **28** 105015
- [28] Raitses Y and Fisch N J 2001 Parametric investigations of a nonconventional Hall thruster *Phys. Plasmas* **8** 2579–86
- [29] Koizumi H *et al* 2016 Initial flight operations of the miniature propulsion system installed on small space probe: PROCYON *Trans. Jpn. Soc. Aeronaut. Space Sci. Aerosp. Technol. Jpn.* **14** b_13–22
- [30] Takahashi K 2019 Helicon-type radiofrequency plasma thrusters and magnetic plasma nozzles *Rev. Mod. Plasma Phys.* **3** 3
- [31] Karabadzak G F, Chiu Y-H and Dressler R A 2006 Passive optical diagnostic of Xe propelled hall thrusters. II. Collisional-radiative model *J. Appl. Phys.* **99** 113305
- [32] Yang J, Yokota S, Kaneko R and Komurasaki K 2010 Diagnosing on plasma plume from xenon hall thruster with collisional-radiative model *Phys. Plasmas* **17** 103504
- [33] Wang Y, Wang Y-F, Zhu X-M, Zatsarinny O and Bartschat K 2019 A xenon collisional-radiative model applicable to electric propulsion devices: I. Calculations of electron-impact cross sections for xenon ions by the dirac B-spline R-matrix method *Plasma Sources Sci. Technol.* **28** 105004
- [34] Zhu X-M, Wang Y-F, Wang Y, Yu D-R, Zatsarinny O, Bartschat K, Tsankov T V and Czarnetzki U 2019 A xenon collisional-radiative model applicable to electric propulsion devices: II. Kinetics of the 6s, 6p and 5d states of atoms and ions in Hall thrusters *Plasma Sources Sci. Technol.* **28** 105005
- [35] Priti, Gangwar R K and Srivastava R 2019 Collisional-radiative model of xenon plasma with calculated electron-impact fine-structure excitation cross-sections *Plasma Sources Sci. Technol.* **28** 025003
- [36] Wang J, Polk J, Brophy J and Katz I 2003 Three-dimensional particle simulations of ion-optics plasma flow and grid erosion *J. Propul. Power* **19** 1192–9
- [37] Summers H P and O'Mullane M G 2011 Atomic data and modelling for fusion: the ADAS project *AIP Conf. Proc.* **1344** 179–87
- [38] Griener M *et al* (The ASDEX Upgrade Team) 2017 Qualification and implementation of line ratio spectroscopy on helium as plasma edge diagnostic at ASDEX Upgrade *Plasma Phys. Control. Fusion* **60** 025008
- [39] Griener M, Wolfrum E, Cavedon M, Dux R, Rohde V, Sochor M, Muñoz Burgos J M, Schmitz O and Stroth U (ASDEX Upgrade Team) 2018 Helium line ratio spectroscopy for high spatiotemporal resolution plasma edge profile measurements at ASDEX Upgrade (invited) *Rev. Sci. Instrum.* **89** 10D102
- [40] Pigarov A Y and Krasheninnikov S I 1996 Application of the collisional-radiative, atomic-molecular model to the recombining divertor plasma *Phys. Lett. A* **222** 251–7
- [41] Fujimoto T 1979 A collisional-radiative model for helium and its application to a discharge plasma *J. Quant. Spectrosc. Radiat. Transfer* **21** 439–55
- [42] Kajita S *et al* 2017 Behavior of 23S metastable state He atoms in low-temperature recombining plasmas *Phys. Plasmas* **24** 073301
- [43] Kajita S, Suzuki K, Tanaka H and Ohno N 2018 Helium line emission spectroscopy in recombining detached plasmas *Phys. Plasmas* **25** 063303
- [44] Nishijima D and Hollmann E M 2007 Determination of the optical escape factor in the He I line intensity ratio technique applied for weakly ionized plasmas *Plasma Phys. Control. Fusion* **49** 791
- [45] Shuker R, Szöke A, Zamir E and Binur Y 1975 Energy transfer in noble-gas mixtures: Penning ionization in He/Xe *Phys. Rev. A* **11** 1187–92
- [46] Santos M, Noël C, Belmonte T and Alves L L 2014 Microwave capillary plasmas in helium at atmospheric pressure *J. Phys. D: Appl. Phys.* **47** 265201
- [47] Raitses Y, Rodriguez E, Skoutnev V, Powis A, Kraus B, Kaganovich I and Smolyakov A 2019 Characterization of the ExB Penning discharge using electrostatic probes *The 36th Int. Electric Propulsion Conf.* p IEC–2019–433
- [48] Skoutnev V, Dourbal P, Rodríguez E and Raitses Y 2018 Fast sweeping probe system for characterization of spokes in $E \times B$ discharges *Rev. Sci. Instrum.* **89** 123501
- [49] Rodríguez E, Skoutnev V, Raitses Y, Powis A, Kaganovich I and Smolyakov A 2019 Boundary-induced effect on the spoke-like activity in $E \times B$ plasma *Phys. Plasmas* **26** 053503
- [50] Frieman J D, Liu T M and Walker M L R 2017 Background flow model of Hall thruster neutral ingestion *J. Propul. Power* **33** 1087–101
- [51] Hamagaki M H M and Hara T H T 1994 Potential profiles in an electron-beam-excited plasma *Jpn. J. Appl. Phys.* **33** 4369
- [52] Godyak V A and Alexandrovich B M 2015 Comparative analyses of plasma probe diagnostics techniques *J. Appl. Phys.* **118** 233302
- [53] Lobbia R B and Beal B E 2017 Recommended practice for use of Langmuir probes in electric propulsion testing *J. Propul. Power* **33** 566–81
- [54] Sasaki S, Takamura S, Watanabe S, Masuzaki S, Kato T and Kadota K 1996 Helium I line intensity ratios in a plasma for the diagnostics of fusion edge plasmas *Rev. Sci. Instrum.* **67** 3521–9
- [55] Kajita S, Nishijima D, Hollmann E M and Ohno N 2009 Ray tracing simulation for radiation trapping of the He I resonance transitions in a linear plasma device *Phys. Plasmas* **16** 063303
- [56] Kajita S and Ohno N 2011 Practical selection of emission lines of He I to determine the photon absorption rate *Rev. Sci. Instrum.* **82** 023501
- [57] Holstein T 1947 Imprisonment of resonance radiation in gases *Phys. Rev.* **72** 1212–33
- [58] Holstein T 1951 Imprisonment of resonance radiation in gases. II *Phys. Rev.* **83** 1159–68
- [59] Phelps A V 1958 Effect of the imprisonment of resonance radiation on excitation experiments *Phys. Rev.* **110** 1362–8
- [60] Dubreuil B and Catherinot A 1978 “Optical escape factor” measurement for the 31P–11S radiative transition in a helium glow discharge by a laser perturbation method *Physica B+C* **93** 408–13
- [61] Otsuka M, Ikee R and Ishii K 1979 Optical escape factors and population densities for TPD-plasma *J. Quant. Spectrosc. Radiat. Transfer* **21** 41–53
- [62] Iida Y, Kado S and Tanaka S 2010 Calculation of spatial distribution of optical escape factor and its application to He I collisional-radiative model *Phys. Plasmas* **17** 123301